Check for updates

Original Article





Validating bond-based peridynamic model using displacement potential approach

Proc IMechE Part C:

J Mechanical Engineering Science
1−10

© IMechE 2022

Article reuse guidelines:
sagepub.com/journals-permissions
DOI: 10.1177/09544062221140342
journals.sagepub.com/home/pic

(\$)SAGE

Jared Rivera, Yuzhe Cao, Longwen Tango and Mathieu Bauchy

Abstract

Although peridynamics is widely used to investigate mechanical responses in materials, the ability of peridynamics to capture the main features of realistic stress states remains unknown. Here, we present a procedure that combines analytic investigation and numerical simulation to capture the elastic field in the mixed boundary condition. By using the displacement potential function, the mixed boundary condition elasticity problem is reduced to a single partial differential equation which can be analytically solved through Fourier analysis. To validate the peridynamic model, we conduct a numerical uniaxial tensile test using peridynamics, which is further compared with the analytic solution through a convergence study. We find that, when the parameters are carefully calibrated, the numerical predicted stress distribution agrees very well with the one obtained from the theoretical calculation.

Keywords

Peridynamics, mixed boundary condition, elasticity, brittle failure, displacement potential approach

Date received: 9 April 2022; accepted: 2 November 2022

Introduction

Understanding the role of mechanical properties and geometric factors in determining the mechanical performance of the materials is crucial for modern engineering, especially in the context of high-tech and structural glasses. Brittle materials, such as glass, can be broken suddenly without any obvious deformation under scratching, impact, or fatigue, which limits their further application. ^{1–7} One of the obstacles to performing structural analysis on materials is the difficulty in determining the in-situ state of stress. This can be characterized by the stress field in the bulk resulting from a given loading. Experimentally, stress fields can be determined with photoelasticity, strain correlations based on strain gauges, and high-speed photometry of dots painted on the sample. ⁸

However, such experimental studies have been limited mainly by two factors, which makes it difficult to analyze the exact role of mechanical properties and geometric factors on material failure. First, the evolution of stress fields during the crack propagation is still difficult to access through experiments due to the limitation of the resolution of devices. As such, most of the experimental measurements can hardly explicitly capture the local details of deformation and corresponding stress during the loading process at small scales. Second, real boundary conditions in terms of loads and displacements are very hard to exactly

determine and constrain in-situ as it requires intensive stress analysis. An example of this is seen in the undesired effects of barreling seen in uniaxial compression testing due to the friction between the specimen and the loading device. ¹⁰ Stress analysis is based on the framework of continuum mechanics, and ever more complex problems continue to be solved with the help of new mathematical methods and computational tools. ^{11–15} These problems are typically approached on the basis of either deformation or stress parameters, which are often used to generate linear systems of equations to solve for wanted unknowns.

Generally, the stress function approach and the displacement potential formulation are two widely used methods for solving boundary value elasticity problems. ^{16,17} The stress function approach had commonly been employed in the finite difference techniques, where all boundary conditions are described as stress or concentrated force. ^{16,18} However, this treatment also results in some limitations as it doesn't

Physics of Amorphous and Inorganic Solids Laboratory, Department of Civil and Environmental Engineering, University of California, Los Angeles, CA, USA

Corresponding author:

Longwen Tang, 3256N Boelter Hall, Department of Civil and Environmental Engineering, University of California, Los Angeles, CA 90095, USA.

Email: whutang@ucla.edu

lend itself well to finding solutions to problems where the boundary conditions are complex. As a result, this method is not suitable for the problems that have rigid components or fixed supports, and thus excludes the stress function approach from being a realistic candidate for solving many practical mixed boundary value problems. In the mixed boundary value problem, the boundary conditions are specified in terms of both force (or stress) and displacement (or strain). Stress fields need to be well understood in a reliable manner in engineering structures for the sake of safety and economic feasibility, leaving the displacement potential formulation as the ideal candidate for general analysis. In this method, the problem is a specific solution to a governing partial differential equation (PDE) of strain equilibrium. The potential function satisfying this equation and the boundary conditions is defined in terms of the spatial variables defining the plane in which the stress field lives. Opportunely, the method has the benefit of reducing the number of dependent variables with respect to finite difference approaches by a half. This results in a massive reduction in effort for finding an analytical solution and higher accuracy without additional problem at zones of transition between types of boundary condition. 16,19-24

The alternative method is turning to numerical simulations, which can provide detailed information at the time and length scale that can hardly be accessible by experiments. The failure of materials has been studied in the past across a large range of length scales: including the electronic scale, ²⁵ the atomic scale, ^{26–29} and the macroscopic scale. ^{30–34} Although the atomic scale simulation can provide more comprehensive insight on the mechanical behavior of materials, 25,35,36 it is computationally expensive and can hardly be employed at macroscopic scale. The finite element method (FEM) is the most widely used to investigate the mechanical behavior of materials at macroscopic scale. However, since the governing equation of FEM is written in the partial differential form, numerical difficulties will occur when the crack emerges and disrupts continuity. As a result, FEM simulation may be problematic when the fracture is not negligible.3

As this issue is inherent to the local treatment of FEM, Silling³⁸ proposed a non-local formulation of the dynamical equations of continuum mechanics inspired by MD³⁹: peridynamics. The advantage of this non-local form is that the continuity of strain or stress field is no longer required, which make it more suitable for the problem where the significant discontinuity is involved, such as blast, ^{40,41} impact, ^{1,42,43} failure of composite materials, ⁴⁴ and crack propagation. ^{42,45}

In the present work, we investigate the stress field within a glass pane using the displacement potential formulation combined with peridynamic simulations. Based on the displacement potential method, we give a stress distribution of the sample under uniaxial loading. To obtain a reliable result, we perform a convergence study for several computational parameters, which are essential for peridynamic simulation. By comparing the stress distribution from the theoretical calculation and peridynamics simulation, we demonstrate the ability of peridynamics to reproduce the accurate mechanical response of materials under realistic boundary conditions. The procedure presented in this study can also be used to validate other peridynamic models and calibrate the corresponding parameters.

Method and algorithm of solution

Peridynamics

Peridynamics was postulated as a reformulation of continuum mechanics, such that it is described by integral equations rather than differential equations. 38,46-49 This removes the necessity of the differentiability of the displacement field, providing valid equations of motion that can describe cracks and discontinuities in extended bodies. 45,50-53 As a continuum model, peridynamics can be discretized by both mesh-free and mesh-based methods. In the case of a uniform grid-style mesh, the domain is discretized into a lattice whereupon particles at the nodes interact by pair-wise forces. This formulation lends itself well to being generalized toward simulating materials with complex constitutive models such as plasticity and viscoelasticity. 47,54 Rather than interacting only with the connected points, the particle can also interact with the particles within the specific region, which is usually a sphere region with a certain radius called the horizon, δ . Accordingly, in peridynamics, the equation of motion is rewritten in the integral form:

$$\rho \ddot{\mathbf{u}}(\mathbf{x};t) = \int_{H_x} \mathbf{f}(\mathbf{u}(\mathbf{x}',t) - \mathbf{u}(\mathbf{x},t), \mathbf{x}' - \mathbf{x}) d\mathbf{x}' + \mathbf{b}(\mathbf{x},t)$$
(1)

where $\mathbf{f}(.)$ describes the force between particles located at \mathbf{x} and \mathbf{x}' (i.e. pairwise force function). $H_{\mathbf{x}}$ represents the region within the horizon. The functional form of $\mathbf{f}(.)$ depends on the material model used. $\ddot{\mathbf{u}}$ is the second derivative of the displacement (i.e. acceleration) vector field, ρ is the mass density, and \mathbf{b} is the applied external force density.

In recent years, various types of peridynamics models and associated material models have been proposed. However, despite its simple nature, the bond-based model has previously been shown to be successful in reproducing the key features of fracture in brittle materials. Here, we focus on the bond-based model in this study. For a prototype microelastic brittle (PMB) bond-based material, **f**(.) can be expressed as: 50

$$f(\mathbf{\eta}, \ \xi \) = \begin{cases} \frac{\xi + \mathbf{\eta}}{\|\xi + \mathbf{\eta}\|} cs, & \|\xi \| \le \delta \\ 0, & \|\xi\| > \delta \end{cases}$$
 (2)

where ξ denotes the displacement of particles and η is interparticle separation. Thus, $\frac{\xi + \eta}{\xi + \eta}$ represents the unit vector of bond stretch. c is the bond constant, and s represents the relative bond stretch. Then, the micromodulus c is given as: 50

$$c = \frac{18K}{\pi\delta^4} \tag{3}$$

where K is the bulk modulus and δ is horizon. The bonds between lattice points are assumed to undergo purely linear elastic deformation until they reach the critical stretch s_0 . Once the elongation is greater than s_0 , the bond will be removed in the simulation to mimic the initiation and propagation of cracks. Based on linear elastic fracture mechanics, the critical bond stretch s_0 is determined according to the energy released during the crack propagation 45 :

$$s_0 = \sqrt{\frac{5G_c}{9K\delta}} \tag{4}$$

where G_c is the fracture energy of the material. Based on that, the damage at a material point \mathbf{x} and time t is defined as

$$\varphi(x,t) = 1 - \frac{\int_{H_x} \mu(t, \mathbf{\eta}, \xi) dV_{x'}}{\int_{H_x} dV_{x'}}$$
 (5)

where $\mu(t, \eta, \xi)$ is a Boolean function, which is equal to 0 when bond is broken, and otherwise is equal to 1. According to this definition, the damage of a point with no broken bonds is 0, and one with all bonds broken will have a damage of 1. Thanks to the nonlocal treatment of the interactions between points within the horizon, the singularity that comes from the discontinuity can be overcome by the integral formation of the motion equation, which avoids complicated remesh or other procedures in traditional FEM.

Analytic model

In this study, the glass plate is in the threedimensional stress state. The pane is subjected to uniaxial tension in y-direction by imposing the constant velocity on the top and bottom boundaries (see Figure 1). To remove the potential rigid rotation, the x- and z-directions are also fixed on the top and bottom boundaries. Beyond that, there is no additional constrain on the pane.

Here, for linear elastic material, the stress can be expressed using the Cauchy stress tensor formulation¹⁷:

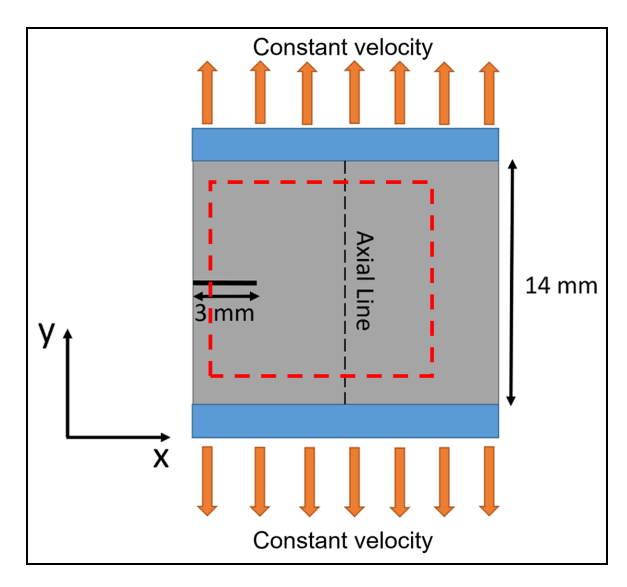


Figure 1. Schematic illustration of boundary condition. The orange arrows indicate the direction of constant velocity. The axial line is located at the middle point of the cross section. The red dashed line is the *J*-integral contour.

$$\begin{pmatrix} \sigma_{x} \\ \sigma_{y} \\ \sigma_{z} \end{pmatrix} = \frac{E}{2\nu^{2} + \nu - 1} \begin{pmatrix} \nu - 1 & -\nu & -\nu \\ -\nu & \nu - 1 & -\nu \\ -\nu & -\nu & \nu - 1 \end{pmatrix} \begin{pmatrix} \varepsilon_{x} \\ \varepsilon_{y} \\ \varepsilon_{z} \end{pmatrix}$$
(6)

$$\sigma_{y} = \frac{E}{2\nu^{2} + \nu - 1} [(\nu - 1)\varepsilon_{y} - \nu(\varepsilon_{x} + \varepsilon_{z})]$$
 (7)

Since material is assumed to be isotropic, we can use the ansatz $\varepsilon_x = \varepsilon_z = -\nu \varepsilon_y f(y)$, where $f(y) \in [0,1]$, with 0 yielding plane strain at the boundaries and 1 yielding plane stress in the center. Then, σ_y can be expressed as:

$$\sigma_{y} = \left(\frac{1 - \nu - 2\nu^{2} f(y)}{1 - \nu - 2\nu^{2}}\right) E \varepsilon_{y}$$
 (8)

To determine the functional form of the y-dependence function, we turn to the displacement potential, which is defined by the governing PDE:¹⁶

$$\frac{\partial^4 \Psi}{\partial x^4} + 2 \frac{\partial^4 \Psi}{\partial x^2 \partial y^2} + \frac{\partial^4 \Psi}{\partial y^4} = 0 \tag{9}$$

where displacement in the y direction is given in terms of the potential:²²

$$u_{y}(x,y) = \frac{1}{1+\bar{v}} \left(2\frac{\partial^{2}\Psi}{\partial x^{2}} + (1-\bar{v})\frac{\partial^{2}\Psi}{\partial y^{2}} \right)$$
(10)

where \bar{v} signifies the effective Poisson ratio defined as:

$$\bar{v} = \begin{cases} \nu, & plane \ stress \\ \frac{\nu}{1-\nu}, & plane \ strain \end{cases}$$
 (11)

Similarly, the effective Young's modulus \bar{E} is defined as:

$$\bar{E} = \begin{cases} E, & plane \ stress \\ \frac{E}{1-\nu^2}, & plane \ strain \end{cases}$$
 (12)

We can then represent the longitudinal stress in terms of the potential:

$$\sigma_{y} = \frac{\bar{E}}{(1+\bar{v})^{2}} \left((2+\bar{v}) \frac{\partial^{3} \Psi}{\partial x^{2} \partial y} + \frac{\partial^{3} \Psi}{\partial y^{3}} \right)$$
(13)

Here, we use the Fourier series representation of Ψ :

$$\Psi(x,y) = \sum_{m=1}^{\infty} Y_m(y)\sin(\alpha x), \ \alpha \equiv \frac{m\pi}{L_x}$$
 (14)

where L_x is the width of the body in the x-direction. Combined with (9) and (14), $Y_m(y)$ can be expressed as:

$$Y_m(y) = A_m \cosh(\beta y) + B_m \beta y \sinh(\beta y) + C_m \sinh(\beta y) + D_m \beta y \cosh(\beta y)$$
(15)

where $\beta = \frac{m\pi}{L_y}$. According to the axial stress, the force boundary condition can be written as:

$$\sigma_{\mathbf{v}}(x,0) = \sigma_{\mathbf{v}}(x, L_{\mathbf{v}}) = P \tag{16}$$

Since the ends are fixed to prohibit motion, we can get another displacement boundary condition:

$$u_{\mathbf{x}}(\mathbf{x},0) = u_{\mathbf{x}}(\mathbf{x}, L_{\mathbf{y}}) = 0$$
 (17)

where

$$u_{\mathbf{x}}(x,y) = \frac{\partial^2 \Psi}{\partial x \partial y} \tag{18}$$

Noted that the ends are regarded as fixed supports since there is no rotation for these supports. These boundary conditions are enough to uniquely characterize the Fourier coefficient equation. Plugging equations (14) and (15) into equation (13), subject to the boundary conditions from equations (17) and (18), yields a proportionality

$$Y_m(y) \sim \sinh^2(y) \tag{19}$$

which in turn yields

$$\sigma_{y} \sim \frac{2\bar{E}(2-\bar{v})}{(1+\bar{v})^{2}} \sum_{m=1}^{\infty} \sinh(\beta y) \cosh(\beta y) \sin(\alpha x)$$
(20)

We now can compare this to the relation derived from the Cauchy stress tensor. Here, we only consider the central longitudinal axis of the pane as we care about the bulk behavior. In this case, $\sin(\alpha x) \approx 1$, which leads to:

$$f(y) \sim \sum_{m=1}^{\infty} \sinh(\beta y) \cosh(\beta y)$$
 (21)

which can be approximated, for $0 \le y \le L_y$, as:

$$f(y) \sim \sinh^2(y) \tag{22}$$

Imposing the constraints on the function known from our physical knowledge of the problem, we find:

$$f(y) = 1 - \sinh^2\left(\frac{y}{y_0}\right), \ y_0 = \frac{L_y}{2\sinh^{-1}(1)}$$
 (23)

Finally resulting in the familiar relationship

$$\sigma_{\rm v} = E(y)\varepsilon_{\rm v} \tag{24}$$

$$E(y) = E\left(1 + \frac{2\nu^2 \sinh^2\left(\frac{y}{y_0}\right)}{1 - \nu - 2\nu^2}\right)$$
 (25)

We can see that $E(y) \to \overline{E}$ for the appropriate values of y. Equation (25) is the key result of this analysis.

The Courant-Friedrichs-Lewy (CFL) condition

The timestep used in peridynamics should be carefully selected to ensure the convergence of simulation. The CFL condition is widely used to select the critical timestep for peridynamics. The basic idea of CFL condition is that the timestep should be shorter than the critical time required for the mechanical wave to go through the lattice spacing.⁵⁵ Here, it can be expressed as:

$$a\frac{\Delta t}{\Delta x} \leqslant 1$$
 (26)

In peridynamics, Δx is the lattice spacing and a can be taken to be the Rayleigh velocity:⁵⁶

$$a = C_{\rm r} = \sqrt{\frac{E}{(1+\nu)\rho}} \tag{27}$$

Simulation input parameter		Material input parameter		Simulation result		% Error
$\delta \Delta x$	$3 \Delta x$ 0.2mm	E (GPa)	95.25	E (GPa)	94.5	0.79
$\dot{\epsilon}_{y} \\ \Delta t$	0.01 s ⁻¹ 0.1 ns	G_c (J/m ²)	4.3	G_c (J/m ²)	4.39	2.09

Table 1. Performance of peridynamic simulations. The parameters are selected based on the convergence results.

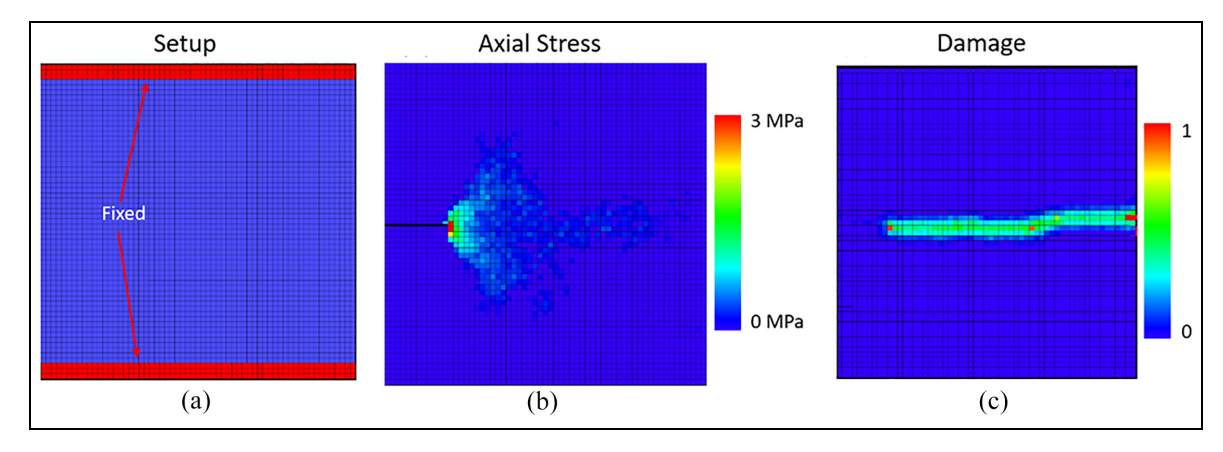


Figure 2. (a) Peridynamics simulation setup before loading. (b) Axial stress at the time when the crack start to propagate, a stress concentration is observed at the crack tip. (c) Counter plot of the damage distribution after failure. The damage value represents the fraction of broken bonds. Crack surface appears when the damage value reach around 0.5.

where ρ is the mass density and E is the Young's modulus. In the PMB model, the Poisson ratio is fixed to be 0.25, so

$$\Delta t \leqslant \Delta x \sqrt{\frac{1.25\rho}{E}} \tag{28}$$

Simulation details

Here, the boundary condition applied in the analytic model is also applied in the numerical model for fair comparison. As shown in the system diagram presented in Figure 1, the length of sample is 14 mm while the out of plane thickness is 3 mm. Moreover, a 3 mm initial infinite sharp crack is created to simulate mode I fracture since the sizes of initial crack and thickness are comparable in many experiments. Noted that, the crack is not created for the simulations where the fracture is not involved. The sample is discretized into lattice point with 0.5 mm lattice spacing. Then, the strain rate $\dot{\varepsilon}$ can be calculated based on the constant velocity v: $\dot{\varepsilon} = \frac{2v}{L}$, where L = 14 mm is the length of the sample.

All of simulations are performed by using the peridynamics package from LAMMPS, which has been validated by comparing the experimental data. 1,2,43,45,57,58 After simulations, the results are further visualized with OVITO. Here, to mimic the brittle materials, the mechanical properties of soda-lime silicate glass are used. 35,42 The input parameters are given in Table 1. Figure 2 shows the implementation at various stages in

LAMMPS: Figure 2(a) shows the initial setup with the glued edges highlighted in red, Figure 2(b) shows the notch in black and the stress concentration that results from the axial load, and Figure 2(c) shows the final crack path by highlighting damaged voxels.

Young's modulus is determined by taking the slope of the stress-strain curve. The stress is determined by setting the *yy*-component of the stress tensor as an output from LAMMPS directly, while the strain is calculated after the simulation from the particle trajectories. For each y-position along the loaded axis of the sample, the Young's modulus is calculated and can be written as the function of *y*-position: E(y). We then fit this E(y) to equation (25) with a chi-square (χ^2) fit taking E as the fitting parameter. The goodness of fit is determined by

$$\chi^2 = \sum_{i=1}^n \frac{(O_i - A_i)^2}{A_i} \tag{29}$$

where O_i is the simulation results and A_i is the analytical results from equation (25). The Young's modulus is determined where χ^2 is minimum.

The fracture energy can be obtained by calculating the area under the stress-displacement curve:⁴⁴

$$G_c = s_0^{\sigma_y} dl_y (30)$$

where σ_y and l_y are the stress and displacement in the loading direction (y-axis), respectively. The term s_0 is calculated based on the system geometry as

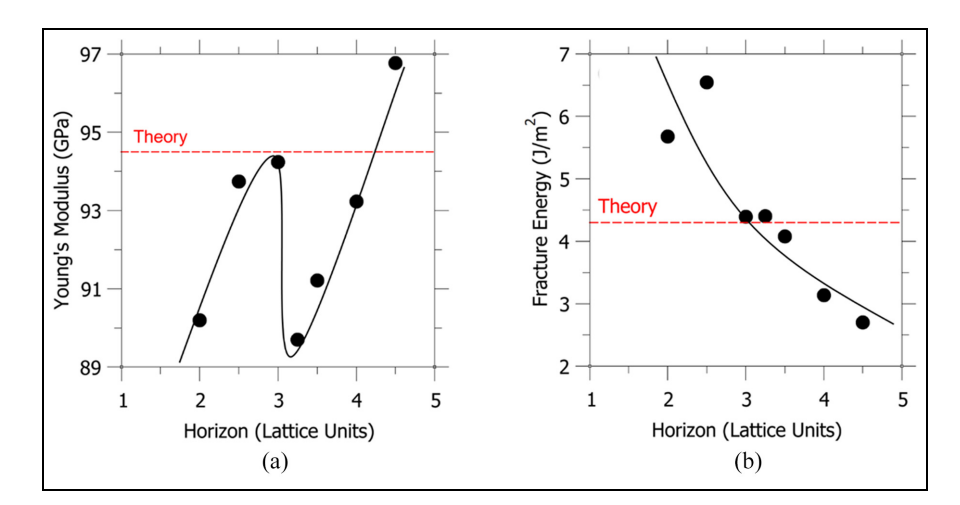


Figure 3. Effect of horizon size on the (a) Young's modulus and (b) fracture energy. The theoretical value informed by the displacement potential formulation and elasticity is shown as a red horizontal line. The black line is a guide for the eye through data points gathered from simulation.

$$s_0 = \frac{L}{L - L_{\rm n}} \tag{31}$$

where L is the length of the specimen and L_n is the length of the notch. Herein, $s_0 = \frac{14}{11}$.

Results and discussion

At beginning, the horizon is selected as three times of lattice spacing. The timestep is 1 ns and the strain rate is 1 s⁻¹. To investigate the effect of horizon size on the simulation results of peridynamics, we vary the size of the horizon from 2 to 4.5 times of lattice spacing while keep the rest simulation parameters unchanged. Noted that the yield stress of brittle material with an initial crack depends on the geometry of the sample and is not compared in this study.

Figure 3(a) shows the calculated Young's modulus as the function of horizon size. The results suggest that there is a non-monotonic relationship between horizon size and Young's modulus. The most accurate Young's modulus obtained from peridynamics can be expected when the horizon size is around 3 and 4.2 times of lattice spacing. Figure 3(b) shows the calculated fracture energy as the function of horizon size. We find that the fracture energy roughly decreases monotonically with the horizon size, while the most accurate fracture energy can be obtained when the horizon size approaches three times of lattice spacing. In each set of figures, the "accuracy" is seen through an agreement with the analytic result informed by the displacement potential formulation which is shown as a red horizontal line. The black line in each set of figures is a guide for the eye through the data points gathered from simulation. The above results suggest that the effect of horizon size is not negligible and the horizon size should be three times of lattice spacing to offer the most accurate mechanical behavior, which agrees with previous studies.^{59,60} Based on that, the horizon size is selected as three times of lattice spacing in the following simulations.

We then investigate the effect of lattice spacing on the simulated mechanical properties. Here, the lattice spacing is varied from 0.1 to 1 mm while the rest of parameters are fixed for a fair comparison.

As shown in Figure 4(a), the significant underestimate of Young's modulus is observed when the lattice spacing becomes comparable with the thickness of the sample. However, the influence of lattice spacing is much smaller when it is less than 0.5 mm. Similarly, the convergence of simulated fracture energy can be observed when the lattice spacing is smaller than 0.5 mm as shown in Figure 4(b). Considering the fact that the decrease of lattice spacing will significantly increase the computational time of peridynamics, the 0.5 mm lattice spacing is selected based on the balance between efficiency and accuracy.

We then investigated the influence of strain rate. To this end, we only vary the velocity of the top and bottom layers to achieve various strain rates without change other simulation details.

Figure 5(a) shows Young's modulus as the function of the strain rate. We found that the extremely high strain rate (i.e. $40\,\mathrm{s}^{-1}$) will overestimate Young's modulus. Nevertheless, the effect of strain rate becomes negligible once it is slower than $0.4\,\mathrm{s}^{-1}$. The influence of strain rate on the fracture energy is also investigated. As shown in Figure 5(b), the simulated fracture energy increase monotonically with strain rate. The origin of this strain rate introduced toughening behavior can be considered as the crack instability under high propagation velocity. Although the fracture energy continues to decrease with strain rate even at $0.4\,\mathrm{s}^{-1}$, the difference of fracture energy caused by strain rate becomes much smaller when it is less than $1\,\mathrm{s}^{-1}$.

Furthermore, we investigate the effect of strain rate on crack propagation. To this end, we first

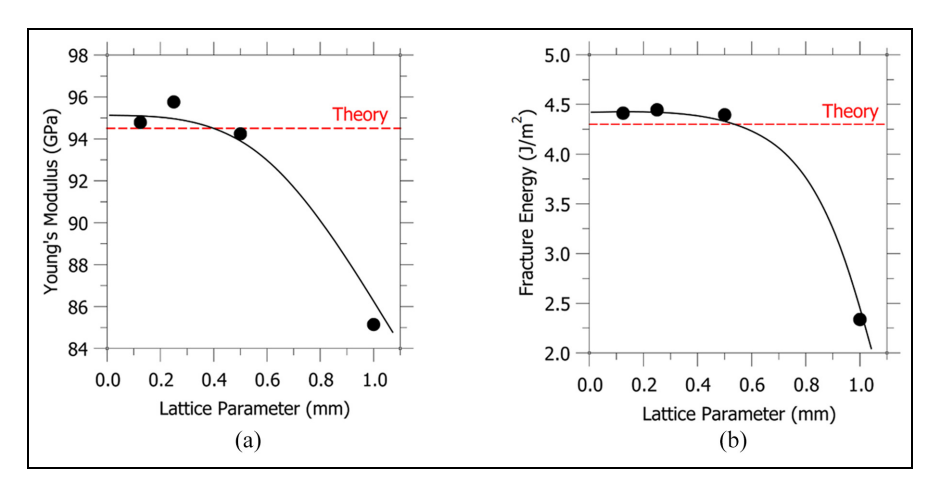


Figure 4. Effect of lattice space on the (a) Young's modulus and (b) fracture energy. The theoretical value informed by the displacement potential formulation and elasticity is shown as a red horizontal line. The black line is a guide for the eye through data points gathered from simulation.

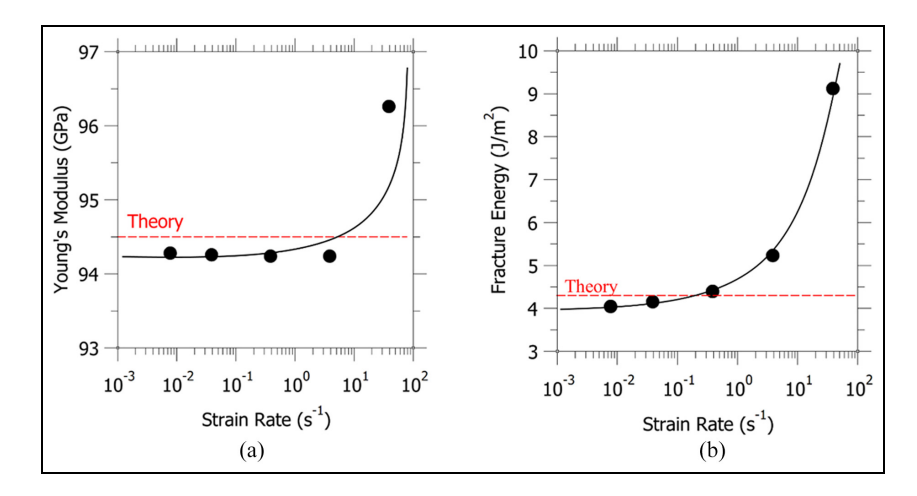


Figure 5. Effect of strain rate on the (a) Young's modulus and (b) fracture energy. The theoretical value informed by the displacement potential formulation and elasticity is shown as a red horizontal line. The black line is a guide for the eye through data points gathered from simulation.

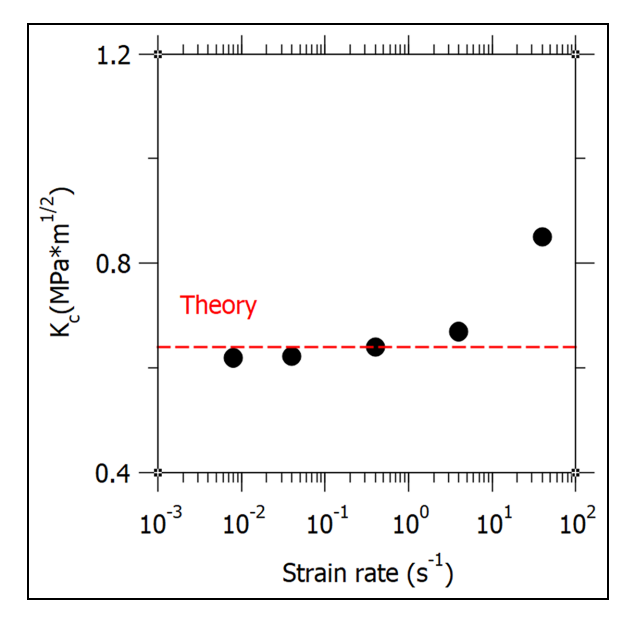


Figure 6. Effect of strain rate on the critical stress intensity factor.

calculated the J-integral based on the method developed in Hu et al.⁶¹ The critical *J*-integral value J_c is recorded as the maximum J-integral value during the loading process.⁶¹ Thus, the critical intensity factor K_c can be expressed as $K_c = \sqrt{EJ_c}$.⁶² As shown in Figure 6, we find that the critical intensity factor K_c increases monotonically with the strain rate. However, this strain rate dependency becomes much less sensitive when the strain rate is lower than 0.4 s⁻¹. In general, to simulate the mechanical behavior under the quasi-static loading condition, the strain rate should be as low as possible. On the other hand, the strain rate should be as high as possible to save computational time. As a result, we select a 0.4 s⁻¹ strain rate to mimic the quasi-static loading condition without significantly increasing the computational cost.

The effect of the timestep is also investigated in this study. Here, the timestep varies from 0.1 to 200 ns while the rest remains consistent. As shown in Figure 7(a), the large timestep (i.e. 200 ns) can significantly

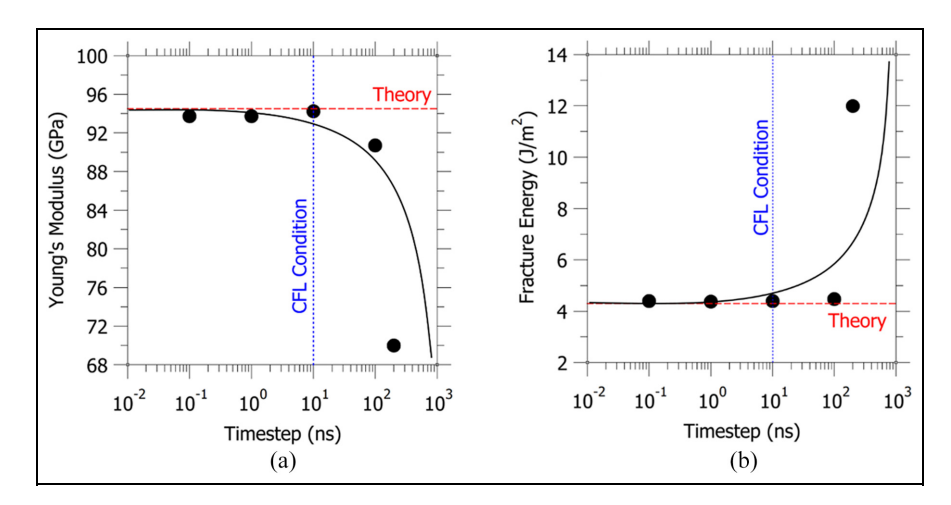


Figure 7. Effect of timestep on the (a) Young's modulus and (b) fracture energy. The theoretical value informed by the displacement potential formulation and elasticity is shown as a red horizontal line. The black line is a guide for the eye through data points gathered from simulation.

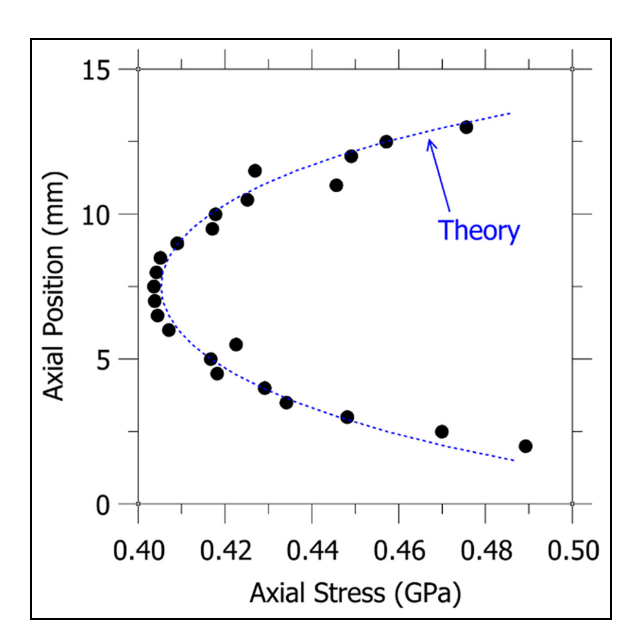


Figure 8. Stress as a function of loading direction along the axial line (depicted in Figure 1). The blue line represents the theoretical results obtained from (24). The black points are obtained from peridynamics simulation.

underestimate Young's modulus. However, the convergence of simulated Young's modulus can be observed once the timestep is smaller than 10 ns, which is in agreement with the CFL condition marked by the vertical blue line. Similarly, the CFL condition can also ensure the convergence of fracture energy as illustrated in Figure 7(b). When the timestep is much larger than the timestep estimated from the CFL condition, the peridynamics simulation can yield unrealistic fracture energy (i.e. three times higher than the theoretical value).

As presented in Table 1, we show that the mechanical properties (i.e. Young's modulus and fracture energy) can be well reproduced by carefully selecting

the simulation parameters (i.e. horizon, lattice spacing, strain rate, and timestep).

Based on that, we now investigate the ability of peridynamics to reproduce the accurate stress field of material under realistic boundaries. Figure 8 shows the local stress along the axial line designated in Figure 1 as the function of the *y*-position. The simulated results show a clear "glued" effect of the regions that are close to the top and bottom boundary: the axial stress decreases monotonically with the distance from the boundary layers and reaches a minimum at the mid-section.

As seen in Figure 8, by comparing the theoretical results from equation (25) (the blue dashed line), we show that the simulated stress distribution (the black points) agrees very well with the theoretical one. Moreover, Table 1 shows the choices of input parameters made based on the convergence study, and shows that the associated simulation output yields excellent agreement with the input Young's modulus and fracture energy when fit to equation (25).

Conclusions

Although peridynamics becomes more popular in recent years, the analytic framework to calibrate the numerical parameters is of critical importance to reproduce reliable simulation results. Rather than comparing with traditional numerical results (such as FEM), we calibrate the parameters for peridynamics by directly comparing them with the theoretic solution. The proposed framework provides a general way to obtain the unphysical numerical parameters in peridynamics that can reproduce the right mechanical properties of brittle materials. Combining the analytic solution with peridynamic simulation, we demonstrate the ability of peridynamics to capture the realistic mechanical behavior of brittle materials under

uniaxial loads. By using the displacement potential function, the mixed boundary condition elasticity problem is reduced to a single partial differential equation which can be analytically solved through Fourier analysis. Then, we perform the peridynamics simulation under the same boundary conditions to validate the reliability of peridynamics. This shows that, when the parameters are carefully calibrated, peridynamics can realistically reproduce the state of stress in the material during loading even for complex boundary conditions, which is necessary for the further implementation of peridynamics. In addition to this, the proposed procedure can also be implemented for more complex peridynamic models (such as advanced models that can capture the fatigue⁶³ or viscoelastic behavior of materials⁶⁴), in which some parameters are not well defined and need to be carefully calibrated. Noted that the current study only considers the tensile fracture (i.e. model I fracture). Extension of the current framework to more complicated loading conditions is necessary in future work. Moreover, with the parameters calibrated by the method proposed in this study, it is also interesting to perform the large-scale peridynamics simulation to investigate the details of crack propagation, such as the evolution of crack velocity and the shape of the crack front.

Declaration of conflicting interests

The author(s) declared no potential conflicts of interest with respect to the research, authorship, and/or publication of this article.

Funding

The author(s) disclosed receipt of the following financial support for the research, authorship, and/or publication of this article: This work was supported by the National Science Foundation (under Grants Nos. 1762292 and 1826420).

ORCID iD

Longwen Tang (b) https://orcid.org/0000-0001-7809-8720

References

- Bobaru F, Ha Y and Hu W. Damage progression from impact in layered glass modeled with peridynamics. *Open Eng* 2012; 2: 551–561.
- 2. Hu W, Wang Y, Yu J, et al. Impact damage on a thin glass plate with a thin polycarbonate backing. *Int J Impact Eng* 2013; 62: 152–165.
- 3. Shi Y, Luo J, Yuan F, et al. Intrinsic ductility of glassy solids. *J Appl Phys* 2014; 115: 043528.
- 4. Mauro JC. Grand challenges in glass science. *Front Mater* 2014; 1: 20.
- 5. Mauro JC and Zanotto ED. Two centuries of glass research: historical trends, current status, and grand challenges for the future. *Int J Appl Glass Sci* 2014; 5: 313–327.

 Mauro JC, Philip CS, Vaughn DJ, et al. Glass science in the United States: current status and future directions. *Int J Appl Glass Sci* 2014; 5: 2–15.

- 7. Wang M, Wang B, Krishnan NMA, et al. Ion exchange strengthening and thermal expansion of glasses: common origin and critical role of network connectivity. *J Non-Cryst Solids* 2017; 455: 70–74.
- Lagattu F, Brillaud J and Lafarie-Frenot M-C. High strain gradient measurements by using digital image correlation technique. *Mater Charact* 2004; 53: 17–28.
- Tang Z, Abrams MB, Mauro JC, et al. High-speed camera study of Stage III crack propagation in chemically strengthened glass. *Appl Phys A* 2014; 116: 471–477.
- Narayanasamy R, Murthy RSN, Viswanatham K, et al. Prediction of the barreling of solid cylinders under uniaxial compressive load. *J Mech Work Technol* 1988; 16: 21–30.
- Conway HD, Chow L and Morgan GW. Analysis of deep beams. J Appl Mech Trans ASME 1951; 18(2): 163–172.
- 12. Murty AVK. Toward a consistent beam theory. *AIAA J* 1984; 22: 811–816.
- Suzuki S. Stress analysis of short beams. *AIAA J* 1986;
 24: 1396–1398.
- Durelli AJ and Ranganayakamma B. Parametric solution of stresses in beams. J Eng Mech 1989; 115: 401–414.
- 15. Hardy SJ and Pipelzadeh MK. Static analysis of short beams. *J Strain Anal Eng Des* 1991; 26: 15–29.
- Deb Nath SK and Reaz Ahmed S. Displacement potential solution of stiffened composite struts subjected to eccentric loading. *Appl Math Model* 2009; 33: 1761–1775.
- 17. Timoshenko SP and Goodier JN. *Elasticity theory* [Russian translation], (Shapiro GS and Nauka M ed.), Springer, 1979.
- 18. Chapel RE and Smith HW. Finite-difference solutions for plane stresses. *AIAA J* 1968; 6: 1156–1157.
- 19. Ahmed S, Khan MR, Islam K, et al. Analysis of stresses in deep beams using displacement potential function. *J Inst Eng India* 1996; 77: 141–147.
- 20. Ahmed SR, Khan MR, Islam KMS, et al. Investigation of stresses at the fixed end of deep cantilever beams. *Comput Struct* 1998; 69: 329–338.
- Akanda MAS, Ahmed SR and Uddin MW. Stress analysis of gear teeth using displacement potential function and finite differences. *Int J Numer Methods Eng* 2002; 53: 1629–1640.
- 22. Ahmed SR, Hossain MZ and Uddin MW. A general mathematical formulation for finite-difference solution of mixed-boundary-value problems of anisotropic materials. *Comput Struct* 2005; 83: 35–51.
- 23. Nath SKD. Displacement potential approach to solution of elasticity problems of orthotropic composite structures, http://lib.buet.ac.bd:8080/xmlui/handle/12345 6789/859 ((2007, accessed 5 July 2020).
- 24. Nath SKD, Ahmed SR and Afsar AM. Displacement potential solution of short stiffened flat composite bars under axial loading, http://www.ijame.uz.zgora.pl/ijame_files/archives/v11PDF/n3/557-575_Article_11.pdf (2006, accessed July 5 2020).
- Chandross M and Argibay N. Ultimate strength of metals. Phys Rev Lett 2020; 124: 125501.
- Samela J and Nordlund K. Classical molecular dynamics simulations of hypervelocity nanoparticle

- impacts on amorphous silica. Phys Rev B 2010; 81: 054108.
- Holmström E, Samela J and Nordlund K. Atomistic simulations of fracture in silica glass through hypervelocity impact. EPL Europhys Lett 2011; 96: 16005.
- Anders C, Bringa EM, Fioretti FD, et al. Crater formation caused by nanoparticle impact: a molecular dynamics study of crater volume and shape. *Phys Rev B* 2012; 85: 235440.
- Saiz F and Gamero-Castaño M. Amorphization of silicon induced by nanodroplet impact: a molecular dynamics study. *J Appl Phys* 2012; 112: 054302.
- Timmel M, Kolling S, Osterrieder P, et al. A finite element model for impact simulation with laminated glass. *Int J Impact Eng* 2007; 34: 1465–1478.
- 31. Krishnan K, Sockalingam S, Bansal S, et al. Numerical simulation of ceramic composite armor subjected to ballistic impact. *Compos Part B Eng* 2010; 41: 583–593.
- Pyttel T, Liebertz H and Cai J. Failure criterion for laminated glass under impact loading and its application in finite element simulation. *Int J Impact Eng* 2011; 38: 252–263.
- Peng Y, Yang J, Deck C, et al. Finite element modeling of crash test behavior for windshield laminated glass. *Int J Impact Eng* 2013; 57: 27–35.
- Doner S, Nayak S, Senol K, et al. Dynamic compressive behavior of metallic particulate-reinforced cementitious composites: SHPB experiments and numerical simulations. *Constr Build Mater* 2019; 227: 116668.
- 35. Wang B, Yu Y, Wang M, et al. Nanoductility in silicate glasses is driven by topological heterogeneity. *Phys Rev B* 2016; 93: 064202.
- Buehler MJ, Abraham FF and Gao H. Hyperelasticity governs dynamic fracture at a critical length scale. *Nature* 2003; 426: 141–146.
- Zienkiewicz OC and Taylor RL. The finite element method for solid and structural mechanics. Elsevier, Butterworth-Heinemann, UK, 2005.
- 38. Silling SA. Reformulation of elasticity theory for discontinuities and long-range forces. *J Mech Phys Solids* 2000; 48: 175–209.
- Seleson P, Parks ML, Gunzburger M, et al. Peridynamics as an upscaling of molecular dynamics. *Multi*scale Model Simul 2009; 8: 204–227.
- Fan H and Li S. A peridynamics-SPH modeling and simulation of blast fragmentation of soil under buried explosive loads. *Comput Methods Appl Mech Eng* 2017; 318: 349–381.
- 41. Wang Q, Wang Y, Zan Y, et al. Peridynamics simulation of the fragmentation of ice cover by blast loads of an underwater explosion. *J Mar Sci Technol* 2018; 23: 52–66.
- Rivera J, Berjikian J, Ravinder R, et al. Glass fracture upon ballistic impact: new insights from peridynamics simulations. Front Mater 2019; 6: 239.
- Parks ML, Lehoucq RB, Plimpton SJ, et al. Implementing peridynamics within a molecular dynamics code. *Comput Phys Commun* 2008; 179: 777–783.
- 44. Tang L, Krishnan NMA, Berjikian J, et al. Effect of nanoscale phase separation on the fracture behavior of glasses: toward tough, yet transparent glasses. *Phys Rev Mater* 2018; 2: 113602.
- Ha YD and Bobaru F. Studies of dynamic crack propagation and crack branching with peridynamics. *Int J Fract* 2010; 162: 229–244.

- Silling SA and Lehoucq RB. Convergence of peridynamics to classical elasticity theory. J Elast 2008; 93: 13.
- 47. Silling SA, Epton M, Weckner O, et al. Peridynamic states and constitutive modeling. *J Elast* 2007; 88: 151–184.
- 48. Silling SA and Lehoucq RB. Peridynamic theory of solid mechanics. In: Aref H and van der Giessen E (eds) *Advances in applied mechanics*. Elsevier, Netherlands, 2010, pp.73–168. DOI: 10.1016/S0065-2156(10) 44002-8.
- Van Le Q and Bobaru F. Objectivity of state-based peridynamic models for elasticity. J Elast 2018; 131: 1–17.
- Silling SA and Askari E. A meshfree method based on the peridynamic model of solid mechanics. *Comput* Struct 2005; 83: 1526–1535.
- 51. Silling SA and Askari E. Peridynamic modeling of impact damage. In: *American society of mechanical engineers digital collection*, San Diego, California, USA, 25–29 July 2004, pp.197–205. New York: *ASME*.
- Foster JT. Dynamic crack initiation toughness: experiments and peridynamic modeling. U.S. Department of Energy Office of Scientific and Technical Information, Oak Ridge, TN, 2009.
- Agwai A, Guven I and Madenci E. Predicting crack propagation with peridynamics: a comparative study. *Int J Fract* 2011; 171: 65.
- Mitchell JA. A non-local, ordinary-state-based viscoelasticity model for peridynamics. U.S. Department of Energy Office of Scientific and Technical Information, Oak Ridge, TN, 2011. DOI: 10.2172/1029821.
- Littlewood DJ, Shelton T and Thomas JD. Estimation of the critical time step for peridynamic models. Sandia National Laboratories SNL-NM, Albuquerque, NM, 2013.
- 56. Sharon E and Fineberg J. Confirming the continuum theory of dynamic brittle fracture for fast cracks. *Nature* 1999; 397: 333–335.
- Plimpton S. Computational limits of classical molecular dynamics simulations. *Comput Mater Sci* 1995; 4: 361–364.
- Parks ML, Seleson P, Plimpton SJ, et al. Peridynamics with LAMMPS: a user guide, v0. 3 Beta, Sandia Rep 2011–8253, 2011. http://prod.sandia.gov/techlib/accesscontrol.cgi/2011/118523.pdf
- 59. Bobaru F and Hu W. The meaning, selection, and use of the peridynamic horizon and its relation to crack branching in brittle materials. *Int J Fract* 2012; 176: 215–222.
- Freimanis A and Paeglitis A. Mesh sensitivity in peridynamic quasi-static simulations. *Proc Eng* 2017; 172: 284–291.
- 61. Hu W, Ha YD, Bobaru F, et al. The formulation and computation of the nonlocal J-integral in bond-based peridynamics. *Int J Fract* 2012; 176: 195–206.
- 62. Griffith AA. VI. The phenomena of rupture and flow in solids. *Phil Trans R Soc Lond A* 1921; 221: 163–198.
- 63. Zhang G, Le Q, Loghin A, et al. Validation of a peridynamic model for fatigue cracking. *Eng. Fract Mech* 2016; 162: 76–94.
- 64. Behera D, Roy P and Madenci E. Peridynamic modeling of bonded-lap joints with viscoelastic adhesives in the presence of finite deformation. *Comput Methods Appl Mech Eng* 2021; 374:3584.